13th International Symposium on Turbulence and Shear Flow Phenomena (TSFP13)
Montreal, Canada, June 25–28, 2024

TOPOLOGY OF FINE SCALE MOTIONS IN A POLYMER DRAG-REDUCED BOUNDARY LAYER

Lucas Warwaruk
Department of Mechanical Engineering
University of Alberta
116 St and 85 Ave, Edmonton, Alberta T6G 2R3 Canada
lwarwaru@ualberta.ca

Sina Ghaemi
Department of Mechanical Engineering
University of Alberta
116 St and 85 Ave, Edmonton, Alberta T6G 2R3 Canada
ghaemi@ualberta.ca

ABSTRACT

The topology of fine scale flow motions are measured in a Newtonian and polymer drag-reduced turbulent boundary layer (TBL) at a common momentum thickness Reynolds number Re_θ of approximately 2300. Compared to the Newtonian TBL, the polymeric boundary layer has a 33% lower skin friction coefficient. Three-dimensional (3-D) particle tracking velocimetry based on the shake-the-box algorithm is used to measure the nine components of the velocity gradient tensor (VGT). The invariants in these tensors are then used to distinguish the topology of different fine scale flow motions – a method referred to as the Δ-criterion (Chong *et al.*, 1990). Few experimental investigations have measured the 3-D structure of fine scale motions in a Newtonian and polymer drag-reduced TBL using the Δ-criterion. Joint probability density functions (JPDFs) of the VGT invariants, Q and R, for the Newtonian TBL demonstrate the well known tear-drop pattern, commonly seen in direct numerical simulations of Newtonian turbulence. Compared to the Newtonian TBL, the polymer drag-reduced flow has significantly attenuated values of R, implying an overall reduction in fluid stretching.

INTRODUCTION

Adding a small amount of high molecular weight polymer to liquid wall-bounded turbulence is a well-established method for reducing the skin friction drag. Since the discovery of polymer drag reduction (DR) by Toms (1948), the phenomenon has garnered considerable attention (Lumley, 1973; White & Mungal, 2008; Xi, 2019); yet, the fundamental question of how polymers reduce drag remains elusive. Older investigations generally involved interpretations of ensemble velocity statistics, such as mean velocity and Reynolds stresses. However, the focus of more recent works has shifted towards understanding the distribution and evolution of coherent flow structures – an analysis driven almost entirely by works using numerical simulations (Xi, 2019). Experimental investigations have trailed in this regard, most likely due to the difficulties involved with measuring coherent structures. Therefore, the main goal of the current investigation is to determine the three-dimensional (3-D) topology of the turbulent motions within a polymer drag-reduced boundary layer using modern flow measurements, in this case 3-D particle tracking velocimetry (3D-PTV) based on the shake-the-box (STB) algorithm. The local topology of the flow will be analyzed using the Δ-criterion, based on the invariants in the velocity gradient tensor (VGT). Evidence is provided to test a hypothesis regarding the mechanism of polymer drag reduction. This hypothesis is inspired by the works of Roy *et al.* (2006) and Lumley (1973) – that being, the large extensional viscosity of polymer solutions strongly inhibits extensional flow regions, thus mitigating the strength and formation of quasi-streamwise vortices and reducing drag. This work provides some of the results of the detailed experimental investigation; however, for a more comprehensive and detailed interpretation of the experimental results, see Warwaruk & Ghaemi (2024).

THEORETICAL BACKGROUND

The Δ-criterion of Chong *et al.* (1990) identifies the topology of fine scale motions within the flow based on the eigenvalues and invariants of the VGT. The VGT is $\mathbf{L} = \nabla \boldsymbol{U}$, and $\boldsymbol{U}$ is the velocity vector. Invariants of $\mathbf{L}$ include P, Q, and R. Although the Δ-criterion can be applied to both compressible and incompressible fluid flows, the present work focuses only on those that are incompressible, thus narrowing down the number of flow classifications. In an incompressible flow, the first invariant $P = -\mathrm{tr}(\mathbf{L})$ is equal to zero, while $Q = -\frac{1}{2}\mathrm{tr}(\mathbf{L}^2)$ and $R = -\det(\mathbf{L})$ are the only non-zero invariants of $\mathbf{L}$. The nature of the eigenvalues of $\mathbf{L}$ are dictated by the sign convention of the discriminant $\Delta = \frac{27}{4}R^2 + Q^3$, where $\Delta > 0$ produces one real and two complex eigenvalues, and $\Delta \leq 0$ produces three real eigenvalues. Figure 1 demonstrates the different possible local flow topologies that depend on the sign convention of Δ and R (Chong *et al.*, 1990). The lines corresponding to $\Delta = 0$, and shown in figure 1, are referred to as the Vieillefosse tail's. Here, ($\Delta = 0$, $R < 0$) is the left-Vieillefosse tail and ($\Delta = 0$, $R > 0$) is the right-Vieillefosse tail. Flow conditions above the Vieillefosse tail's with $\Delta > 0$, consist of motions that are focal and primarily vortical. Regions of the flow with $\Delta \leq 0$ take on

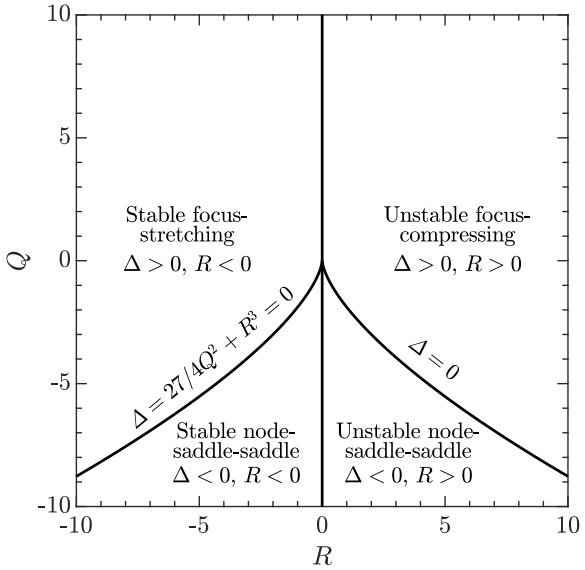

Figure 1. Local topologies for different R and Q in an incompressible flow with $P = 0$ (Chong *et al.*, 1990).

a node-saddle-saddle streamline pattern. Flow topology is also divided about the $R = 0$ axis, where flows with $R < 0$ are stable (stretching) and $R > 0$ are unstable (compressing). JPDFs of Q and R in various Newtonian turbulent flows take on a tear-drop pattern (Soria *et al.*, 1994; Blackburn *et al.*, 1996; Chong *et al.*, 1998; Ooi *et al.*, 1999; da Silva & Pereira, 2008). The point or tip of the tear-drop falls on the right-Vieillefosse tail ($\Delta = 0$, $R > 0$), while the bulb of the tear-drop is situated in the quadrant of stable focus-stretching ($\Delta > 0$, $R < 0$).

EXPERIMENTAL METHODOLOGY

The invariants in the VGT of a Newtonian and polymer-laden turbulent boundary layer were computed using velocity vectors measured from 3-D particle tracking velocimetry (3D-PTV) based on the shake-the-box (STB) algorithm developed by Schanz *et al.* (2016). Newtonian and polymer-laden flows were compared at a similar momentum thickness Reynolds number Re_θ. A description of the flow facility, polymer solution, measurement apparatus and flow computations are provided in the following sections. However, a more detailed explanation of the experimental methodology can be found in Warwaruk & Ghaemi (2024).

Flow Facility

Newtonian and polymer-laden turbulent boundary layers (TBLs) were formed along the floor of a closed-loop water flume. The flume consists of a 5 m long channel that bridges two cubic reservoirs. The channel was 0.68 m in width W. The free surface was situated at a height H that was 0.2 m above the bottom floor of the channel. The total volume of liquid within the flume was 3500 l. Two centrifugal pumps (Deming 4011 4S, Crane Pumps and Systems) in a parallel configuration were used to circulate the fluid within the flume. Measurements of the TBL of water were collected at a free-stream velocities U_∞ of 0.247 m s^{-1}, which produces a Newtonian flow with a boundary layer thickness δ of 78 mm, skin friction coefficient C_f of 3.22×10^{-3} and Re_θ of 2257. The flexible polymer polyacrylamide (PAM) (6030S, SNF Floerger) with a molecular weight of 30-35 MDa, was chosen for the polymer-laden boundary layer experiments. A homogeneous PAM solution

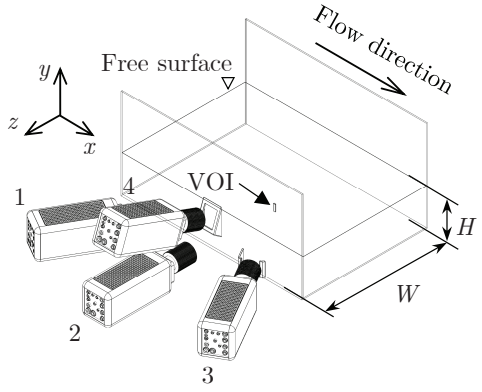

Figure 2. A schematic of the 3D-PTV flow measurement setup with reference to a section of the water channel.

with a concentration c of 140 ppm was utilized. Measurements of the polymer-laden flow were performed at a U_∞ of 0.432 m s^{-1}. The resulting δ was 94 mm, C_f was 2.16×10^{-3}, and Re_θ was 2290. Therefore, the PAM flows has a 33% lower C_f than water at a similar Re_θ.

3-D Particle Tracking Velocimetry

To obtain 3D measurements of the velocity vector $\boldsymbol{U}$ within the Newtonian and non-Newtonian TBLs, 3D-PTV using the STB algorithm was used (Schanz *et al.*, 2016). A schematic of the four-camera 3D-PTV setup is shown in figure 2 with respect to a section of the water flume. An Nd:YLF laser was used to illuminate 2 µm diameter silver-coated glass spheres that were seeded with the flow. The resulting volume of interest (VOI) was $(3.0, 35.8, 8.0)$ mm^3 in size along the streamwise x, wall-normal y and spanwise z directions, respectively. The velocities of the Lagrangian trajectories derived from 3D-PTV are projected onto an Eulerian grid at each instance of time t, effectively producing 3-D time resolved measurements of $\boldsymbol{U}$. A moving first-order polynomial surface was fitted to the velocity components at each instance of time and then differentiated to obtain spatial gradients in velocity. Spatial velocity gradients were then used to compute the topology parameters of the Newtonian and non-Newtonian TBLs.

For the Newtonian and non-Newtonian flows, eight datasets, equivalent to 114,832 images, were collected to ensure sufficient convergence of the different ensemble statistics in the analysis. One time-resolved dataset, for both measurements of the Newtonian and non-Newtonian turbulent boundary layers, consisted of 14,354 single-frame images captured at a selected frequency between 0.52 kHz and 1.82 kHz. Therefore, one dataset took between 7.9 s and 27.6 s. This is equivalent to $36.2T$ and $62.7T$, where $T = \delta/U_\infty$ is a representative advection time or large eddy turnover time, and δ is the boundary layer thickness. The total duration of the eight datasets used for computing ensemble statistics was between $260T$ to $500T$ depending on the flow condition. The frequency was selected depending on U_∞, and such that a maximum particle displacement of 5 pixels across subsequent images was achieved. Image processing consisted of first determining the minimum intensity of each pixel over the complete image ensemble, and then subtracting the minimum from all images in a dataset. Second, the intensity signal at each pixel was normalized by the average intensity of the ensemble. Lastly, a moving local minimum was calculated and subtracted within a kernel

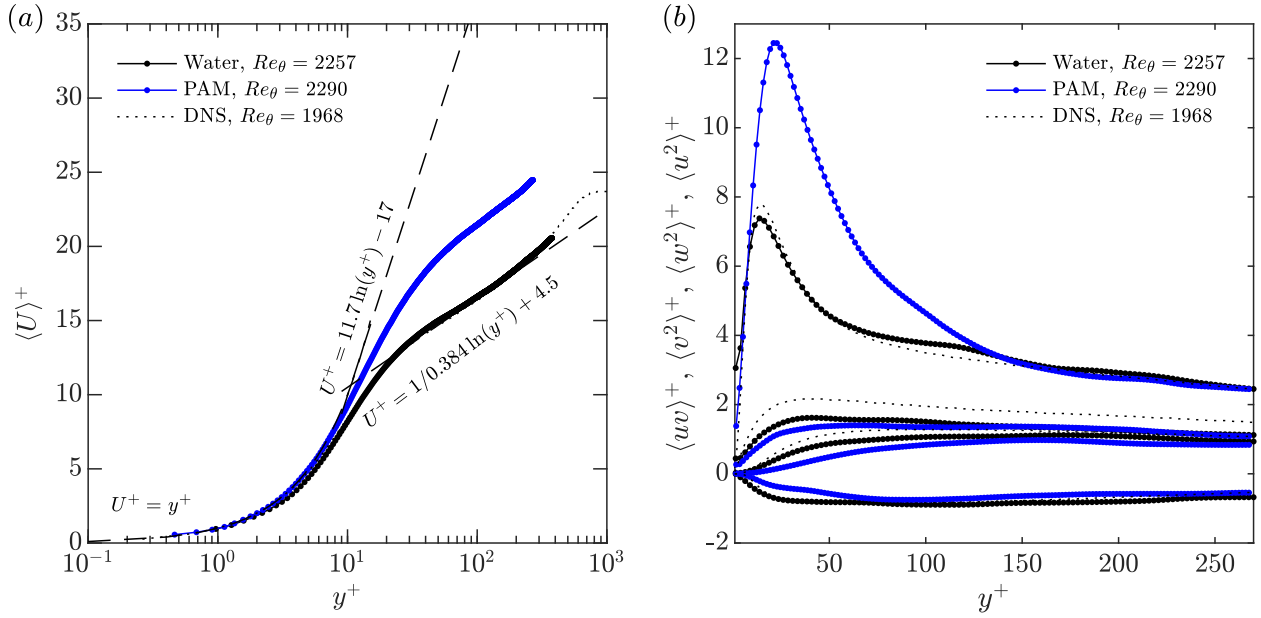

Figure 3. Plots of the (*a*) mean velocity, and (*b*) Reynolds stress profiles for the turbulent boundary layer flow of water and the 140 ppm PAM solution. The dotted lines are mean velocity and Reynolds stress profiles of Newtonian turbulent boundary layer obtained from DNS of Jiménez *et al.* (2010) at $Re_\theta = 1968$.

size of 5 pixels and local intensity normalization with a kernel size of 500 pixels were applied to every image. After image processing, the STB algorithm was performed using DaVis 10.2 software (LaVision GmbH). The maximum triangulation error was set to 1 voxel, and particle displacements were limited to a maximum of 8 voxel. Particles with an acceleration that was larger than 2 pixels or 20% between subsequent image frames were discarded. The STB algorithm yielded approximately 6200 Lagrangian trajectories per time step within the VOI.

Two types of binning were used to convert the Lagrangian trajectories into Eulerian vector components. The first involved averaging the trajectories within slabs that were parallel with the wall and covered the entire measurement domain along x and z. Each slab was 6 voxels or 0.18 mm ($1.3\delta_v - 1.8\delta_v$) thick in the $y-$direction. Neighbouring slabs along y overlapped by 75%. This binning procedure was used exclusively for establishing the mean streamwise velocity $\langle U \rangle$ with high spatial resolution. Here, the angle brackets $\langle \cdots \rangle$ denote averaging in time and along the spatially homogeneous direction z. It was also assessed that $\langle U \rangle$ did not vary significantly along x within the VOI; hence, the statistics were also averaged along the $x-$direction within the VOI. The second binning procedure involved averaging particle tracks for each time step in $32\times32\times32$ voxel or $0.94\times0.94\times0.94$ mm^3 cubes to obtain the instantaneous velocity vector $\boldsymbol{U}$ within the domain. Neighbouring cubes had 75% overlap with one another along the three Cartesian directions. Therefore, adjacent vectors were separated by 8 voxels or 0.235 mm. In terms of viscous wall units $\delta_v = \nu/u_\tau$, the bins were between $6.9\delta_v \times 6.9\delta_v \times 6.9\delta_v$ and $9.3\delta_v \times 9.3\delta_v \times 9.3\delta_v$ depending on the flow considered. Here, u_τ is the friction velocity and ν is the kinematic viscosity. The streamwise, wall-normal and spanwise components of the instantaneous velocity $\boldsymbol{U}$ are denoted as U, V and W, respectively. Velocity fluctuations were represented using lower case symbols, i.e., u, v and w.

A moving first-order polynomial function was fitted to the velocity components at each instance of time and then differentiated to obtain spatial gradients in velocity. The size or extent of the polynomial function was three velocity vector components along each Cartesian direction, which equates to $24\times24\times24$ voxels or $0.70\times0.70\times0.70$ mm^3. Spatial velocity gradients were then used to compute the topology parameters of the Newtonian and non-Newtonian turbulent boundary layers shown in figure 1.

RESULTS

The results of the 3D-PTV flow measurements, involving the Newtonian and polymer-laden boundary layers, are presented in two parts. First, more conventional ensemble statistics such as mean velocity profiles and Reynolds stresses are shown. After which, the $\Delta-$criterion is used to comment on the topology of each flow.

Ensemble Velocity Statistics

Figure 3(*a*) demonstrates inner-normalized mean streamwise velocity $\langle U \rangle^+$ with respect to y^+ for the experimentally measured turbulent boundary layers of water with $Re_\theta = 2257$ and the PAM solution at $Re_\theta = 2290$. Here the superscript + represents normalization by inner-scaling variables – position variables (e.g. y) are normalized by δ_v and velocity is normalized by u_τ. These experimental $\langle U \rangle^+$ profiles are shown alongside the mean velocity profile derived from Newtonian turbulent boundary layer direct numerical simulation (DNS) in Jiménez *et al.* (2010) at an Re_θ of 1968, and also the law of the wall. All flows, both water and PAM, closely follow the linear viscous sublayer $\langle U \rangle^+ = y^+$ for $y^+ < 3$. For $y^+ > 30$ the boundary layers of water with different Re_θ both overlap with a logarithmic profile $\langle U \rangle^+ = 1/\kappa \ln(y^+) + B$ that has a von Kármán coefficient κ of 0.384 and an intercept B of 4.5 – similar to the values prescribed by Nagib & Chauhan (2008) for Newtonian turbulent boundary layers. The polymer-laden flow exhibits enhanced values of $\langle U \rangle^+$ relative to the Newtonian boundary layers for $y^+ > 30$, a feature common in drag-reduced flows of polymer solutions (Warholic *et al.*, 1999). The intercept B of the polymer-laden boundary layer is larger than B for water,

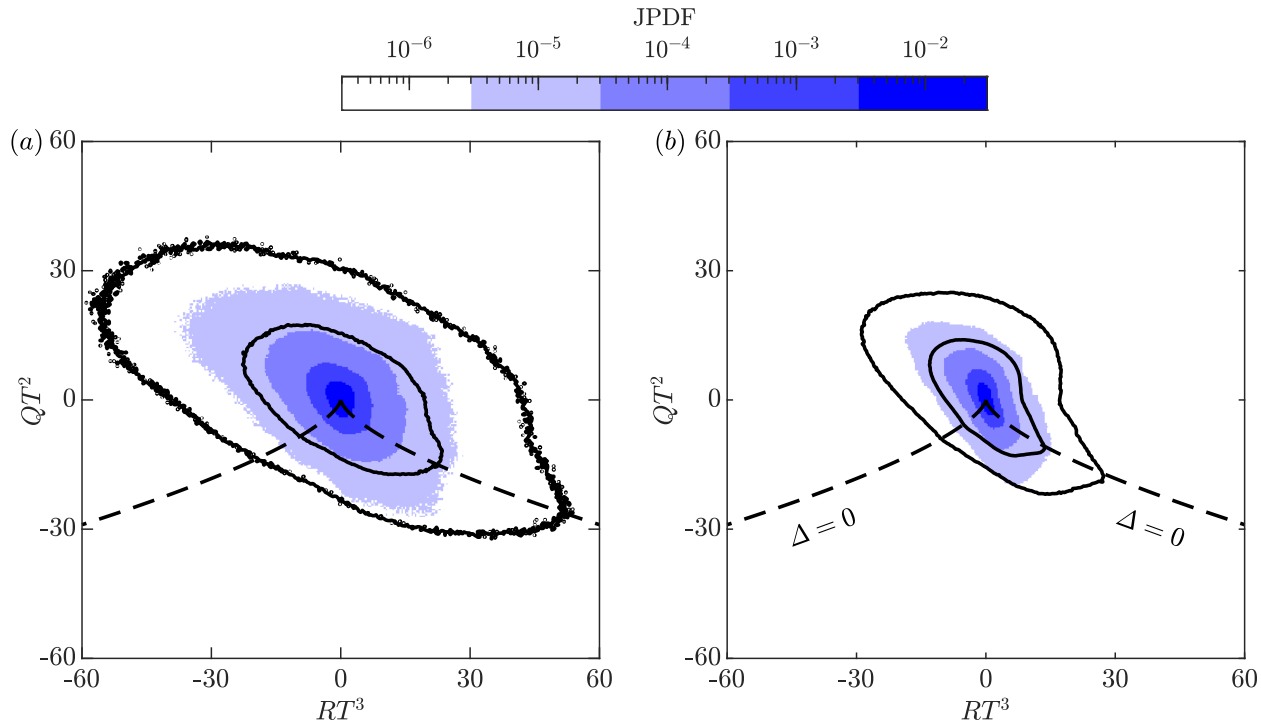

Figure 4. Joint probability density functions of the invariants in the VGT Q and R. The JPDFs in (a) correspond to the buffer layer $3 < y^+ < 30$, and (b) the log layer $y^+ > 30$ and $y/\delta < 0.3$. Filled contours are the JPDFs of PAM, while the open black contours are the JPDFs of water levels of 10^{-5} and 10^{-4}. All gradients are normalized with the large eddy turnover time T. The black dashed line represents $\Delta = 0$.

and visually κ is approximately the same. Although $\langle U\rangle^+$ is enhanced within the outer layer of the polymer-laden flow, it does not overlap with the maximum drag reduction asymptote $\langle U\rangle^+ = 11.7\ln(y^+) - 17.0$ of Virk *et al.* (1970).

Figure 3(b) demonstrates inner-normalized plots of the four non-zero components of the Reynolds stress tensor with respect to y^+. In descending order of magnitude, $\langle u^2\rangle^+$, $\langle w^2\rangle^+$ and $\langle v^2\rangle^+$ are the streamwise, spanwise and wall-normal Reynolds stresses respectively, and $\langle uv\rangle^+$ is the Reynolds shear stress. The experimentally measured profiles of $\langle u^2\rangle^+$, $\langle v^2\rangle^+$ and $\langle uv\rangle^+$ for water overlap well with the DNS of Jiménez *et al.* (2010) at a comparable Re_θ. However, the measured Reynolds stress profiles of $\langle w^2\rangle^+$ for water are marginally less than that of the Newtonian DNS. That being said, profiles of $\langle w^2\rangle^+$ for water with slightly different Re_θ only show subtle difference and rather consistent with one another. The discrepancy among DNS and the measured profiles of $\langle w^2\rangle^+$ is attributed to experimental uncertainties. Measurements of the out-of-plane velocity component, in this case W, are generally more erroneous using 3D-PTV, hence errors in $\langle w^2\rangle^+$ are more expected (Warwaruk & Ghaemi, 2021). Overall, the polymer-laden boundary layer has augmented values of $\langle u^2\rangle^+$ for $y^+ < 150$ and attenuated values of $\langle w^2\rangle^+$, $\langle v^2\rangle^+$ and $-\langle uv\rangle^+$ for $y^+ < 100$, when compared with the boundary layers of water. The peak in $\langle u^2\rangle^+$ is also shifted away from the wall for the PAM flow relative to water; for PAM, the peak in $\langle u^2\rangle^+$ is at a y^+ of 21, while for both of the water flows, the peak in $\langle u^2\rangle^+$ is at a y^+ of approximately 13. These observations are consistent with prior results of polymer drag-reduced flows with similar low drag reduction percentages (Warholic *et al.*, 1999).

Flow Topology

JPDFs of the invariants of $\mathbf{L}$ are shown in figure 4 for the Newtonian and polymer-laden boundary layers at different wall-normal regions of the flow. Open contours with black solid lines in figure 4 are JPDFs of water with an Re_θ of 2257, and equal to 10^{-5} and 10^{-4}. While the blue filled contours represent JPDFs of the PAM boundary layer. Figure 2(a) provides the JPDF of Q and R within the conventional Newtonian limits of the buffer layer, $3 < y^+ < 30$. Velocity gradients are normalized by a large eddy turnover time $T = \delta/U_\infty$. Compared to the flow of water at a similar Re_θ, the PAM boundary layer has attenuated values of Q and R. The range in possible R values narrows considerably compared to water – almost a two fold reduction in the largest magnitude of R. A narrower range in R was similarly observed by Mortimer & Fairweather (2022) for drag-reduced viscoelastic channel flows at a friction Reynolds number of 180 and derived from DNS. This is indicative that stretching and extensional motions within the flow are diminished. Furthermore, the narrowing of Q demonstrates that strong vortical and dissipative motions are less common.

Moving away from the wall, figure 4(b) demonstrates the JPDF of Q and R for $y^+ > 30$ and $y/\delta < 0.3$. Again, open black contours are water, and blue filled contours are the polymer-laden boundary layer at a similar Re_θ. Comparing the JPDFs of water in the buffer layer, figure 4(a), to the log layer, figure 4(b), the strength of the velocity gradients diminishes with increasing distance from the wall and the range of possible Q and R values decreases, i.e., the pattern shrinks. Within the log layer, figure 4(b) demonstrates that the shape of the JPDF in Q and R takes on a more well-defined tear-drop pattern with a clear point at the right-Vieillefosse tail ($\Delta = 0$, $R > 0$) compared to the JPDF of the buffer layer in figure 4(a). Similar observations were made for JPDFs of Q and R based on New-

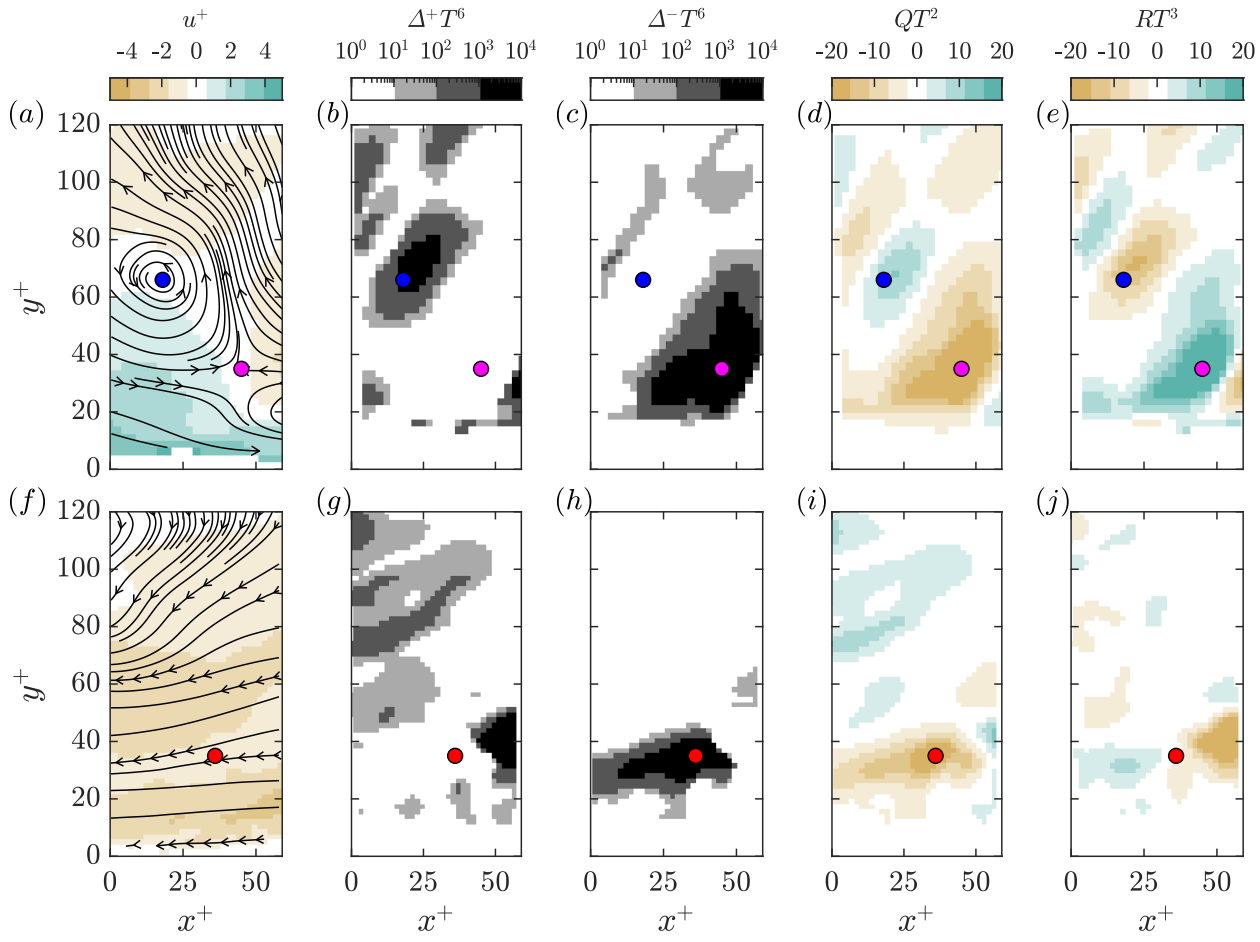

Figure 5. Instantaneous snapshots of u^+ (*a, f*), positive Δ (*b, g*), negative Δ (*c, h*), Q (*d, i*) and R (*e, j*) for the boundary layer of water with an $Re_\theta = 2257$ and PAM. The upper row of figures (*a–e*) is the water flow, and the lower row (*f–j*) is PAM. The snapshots are shown along the $xy-$plane at $z = 1.5$ mm, or the middle of the VOI. The blue dot indicates the spatial location $(x^+, y^+) = (18, 63)$, the magenta dot is $(x^+, y^+) = (45, 35)$, and the red dot is $(x^+, y^+) = (36, 35)$. Black lines in (*a*) and (*f*) are streamlines.

tonian boundary layer DNS in Chong *et al.* (1998). For the PAM boundary layer, the same reduction in the magnitude of Q and R relative to water is still present within the log layer. This is despite the similar Reynolds stresses seen within the log-layer shown in figure 3(*b*). Furthermore, the tear-drop pattern no longer exists in the JPDF of Q and R for PAM, and a well-defined tip does not appear along the right-Vieillefosse tail.

Sample Flow Topologies

The topology of fine scale motions within the boundary layers of PAM and water are unique, as shown by the JPDFs of Q and R in figure 4. To provide a more visual depiction of the differences in the topologies of each flow, the following section demonstrates sample velocity fields for the Newtonian and polymer-laden boundary layers alongside contours of positive and negative regions of Δ, and the VGT invariants Q and R.

An instantaneous snapshot of u^+ and streamlines along an $xy-$plane situated at $z = 1.5$ mm, is shown in figure 5(*a*) for the boundary layer of water at an Re_θ of 2257. Corresponding contours of positive regions of Δ, negative regions of Δ, Q, and R, are shown in figure 5(*b, c, d, e*) respectively. Values of Δ cover a wide range from -10^5 to $+10^5$; hence, contours of Δ are shown on a log-scale, and positive and negative Δ are presented separately as Δ^+ and Δ^-, respectively. The particular instance, shown in figure 5(*a–e*), demonstrates a visibly focal (or vortical) flow region at $(x^+, y^+) = (18, 63)$ indicated by the blue marker. Below the vortex, there is a dissipative region (or node-saddle-saddle) at $(x^+, y^+) = (45, 35)$, indicated with a magenta marker in figure 5(*a–e*). Regarding the blue marker, streamlines in figure 5(*a*) form a spiral pattern that implies large spanwise vorticity. In the neighbouring spatial locations of the blue marker, figure 5(*b*) shows large positive Δ and figure 5(*d*) shows large positive Q, similarly implying the flow is vortical. Furthermore, values of R near the blue marker, shown in figure 5(*e*), are negative, implying the vortex is stretching. Hence, the flow region indicated by the blue marker would constitute a zone of stable-focus-stretching that would fall in the upper-left-hand region of figure 1. On the other hand, the flow region indicated by the magenta marker has streamlines that form a saddle point, as seen in figure 5(*a*). The flow region is indeed dissipative, as confirmed by the large negative Δ, shown in figure 5(*c*), and negative Q, seen in figure 5(*d*). This same region is also in biaxial extension, as demonstrated by the large positive value of R at the location of the magenta marker shown in figure 5(*e*). This region of large biaxial extension is situated at the interface of a high-speed zone ($u^+ > 0$) at $x^+ < 50$, and a low-speed zone ($u^+ < 0$) at $x^+ > 50$, as seen in figure 5(*a*).

Another instantaneous snapshot of u^+, overlaid with 2-D streamlines, along an $xy-$plane situated at $z = 1.5$ mm, is shown in figure 5(*f*) for the boundary layer of PAM at an Re_θ

of 2290. Corresponding contours of Δ^+, Δ^-, Q and R are shown in figure 5(*g, h, i, j*), respectively. Here, a region of the flow that is strongly dissipative (large Δ^-) is emphasized. The particular event is a shear-dominant region that is located at $(x^+, y^+) = (36, 35)$ and denoted using a red marker in figure 5(*f–j*). This region has relatively parallel streamlines in figure 5(*f*), which is characteristic of shear flow. Correspondingly, values of Δ and Q are largely negative around the region of the flow indicated by the red marker, as shown in figure 5(*g–i*). Values of R are also small in magnitude at $(x^+, y^+) = (36, 35)$ and approximately equal to zero, implying the flow is more 2-D, and again, consistent with the appearance of shear flow in figure 5(*a*).

CONCLUSION

The present experimental investigation compared the distribution of fine scale motions within a polymer-laden and Newtonian TBL using three-dimensional particle tracking velocimetry (3D-PTV) and the Δ-criterion of Chong *et al.* (1990). The polymer-laden and Newtonian TBLs had a similar momentum thickness based Reynolds number Re_θ of approximately 2300; however, the polymeric flow had a 33% lower skin friction coefficient. Joint probability density functions (JPDFs) of the invariants in the velocity gradient tensor were used to establish a distribution of the different fine scale motions within the polymer-laden and Newtonian boundary layers, some of which include dissipative (node-saddle-saddle) and vortical (focal) flow motions.

Unambiguous difference in the JPDFs of the invariants in the velocity gradient tensor, Q and R, were observed between the polymer-laden and Newtonian boundary layers. The JPDFs of Q and R for the Newtonian boundary layers exhibited the well-known tear-drop shaped pattern with a clear ridge at the right-Vieillefosse tail. Relative to the Newtonian flows, the polymer-laden boundary layer had attenuated values of Q and R; although values of R were diminished much more than Q. Instantaneous samples of the fine scale motions demonstrate that the dominant dissipative flow motions within the Newtonian boundary layer are extensional, exhibiting a saddle point where streamlines converge. On the other hand, dissipative straining motions within the polymer-laden boundary layer are more shear-dominant, exhibiting small values R closer to zero. For a additional results and details of the experimental investigation, readers are encouraged to consult the work of Warwaruk & Ghaemi (2024).

REFERENCES

Blackburn, H. M., Mansour, N. N. & Cantwell, B. J. 1996 Topology of fine-scale motions in turbulent channel flow. *J. Fluid Mech.* **310**, 269–292.

Chong, M. S., Perry, A. E. & Cantwell, B. J. 1990 A general classification of three-dimensional flow fields. *Phys. Fluids A* **2** (5), 765–777.

Chong, M. S., Soria, J., Perry, A. E., Chacín, J., Cantwell, B. J. & Na, Y. 1998 Turbulence structures of wall-bounded shear flows found using dns data. *J. Fluid Mech.* **357**, 225–247.

Jiménez, J., Hoyas, S., Simens, M. P. & Mizuno, Y. 2010 Turbulent boundary layers and channels at moderate reynolds numbers. *J. Fluid Mech.* **657**, 335–360.

Lumley, J. L. 1973 Drag reduction in turbulent flow by polymer additives. *J. Polym. Sci.* **7**, 263–290.

Mortimer, L. F. & Fairweather, M. 2022 Prediction of polymer extension, drag reduction, and vortex interaction in direct numerical simulation of turbulent channel flows. *Phys. Fluids* **34** (7), 073318.

Nagib, H. M. & Chauhan, K. A. 2008 Variations of von kármán coefficient in canonical flows. *Phys. Fluids* **20** (10), 101518.

Ooi, A., Martin, J., Soria, J. & Chong, M. S. 1999 A study of the evolution and characteristics of the invariants of the velocity-gradient tensor in isotropic turbulence. *J. Fluid Mech.* **381**, 141–174.

Roy, A., Morozov, A., van Saarloos, W. & Larson, R. G. 2006 Mechanism of polymer drag reduction using a low-dimensional model. *Phys. Rev. Lett.* **97** (23), 234501.

Schanz, D., Gesemann, S. & Schröder, A. 2016 Shake-the-box: Lagrangian particle tracking at high particle image densities. *Exp. fluids* **57**, 1–27.

da Silva, C. B. & Pereira, José C.F. 2008 Invariants of the velocity-gradient, rate-of-strain, and rate-of-rotation tensors across the turbulent/nonturbulent interface in jets. *P. fluids* **20** (5), 055101.

Soria, J., Sondergaard, R., Cantwell, B. J., Chong, M. S. & Perry, A. E. 1994 A study of the fine-scale motions of incompressible time-developing mixing layers. *Phys. Fluids* **6** (2), 871–884.

Toms, B. A. 1948 Some observations on the flow of linear polymer solutions through straight tubes at large reynolds numbers. *1st International Congress on Rheology* **2**, 135–141.

Virk, P. S., Mickley, H. S. & Smith, K. A. 1970 The ultimate asymptote and mean flow structure in toms' phenomenon. *ASME. J. Appl. Mech.* **37** (2), 488–493.

Warholic, M. D., Massah, H. & Hanratty, T. J. 1999 Influence of drag-reducing polymers on turbulence: effects of reynolds number, concentration and mixing. *Exp. Fluids* **27** (5), 461–472.

Warwaruk, L. & Ghaemi, S. 2021 A direct comparison of turbulence in drag-reduced flows of polymers and surfactants. *J. Fluid Mech.* **917**, A7.

Warwaruk, L. & Ghaemi, S. 2024 Local flow topology of a polymer-laden turbulent boundary layer. *J. Fluid Mech.* **983**, A22.

White, C. M. & Mungal, M.G. 2008 Mechanics and prediction of turbulent drag reduction with polymer additives. *Ann. Rev. Fluid Mech.* **40**, 235–256.

Xi, L. 2019 Turbulent drag reduction by polymer additives: Fundamentals and recent advances. *Phys. Fluids* **31**, 121302.